

# Measurements and code comparison of wave dispersion and antenna radiation resistance for helicon waves in a high density cylindrical plasma source

D. A. Schneider, G. G. Borg,<sup>a)</sup> and I. V. Kamenski

*Plasma Research Laboratory, Research School of Physical Sciences and Engineering, Australian National University, Canberra, Australian Capital Territory, 0200 Australia*

(Received 13 January 1998; accepted 10 November 1998)

Helicon wave dispersion and radiation resistance measurements in a high density ( $n_e \approx 10^{19} - 10^{20} \text{ m}^{-3}$ ) and magnetic field ( $B < 0.2 \text{ T}$ ) cylindrical plasma source are compared to the results of a recently developed numerical plasma wave code [I. V. Kamenski and G. G. Borg, *Phys. Plasmas* **3**, 4396 (1996)]. Results are compared for plasmas formed by a double saddle coil antenna and a helical antenna. In both cases, measurements reveal a dominance of the  $m = +1$  azimuthal mode to the exclusion of most other modes; in particular, no significant  $m = -1$  mode was observed. The helical antenna, designed to launch  $m < 0$  and  $m > 0$  modes in opposite directions along the field, resulted in an axially asymmetric discharge with very little plasma on the  $m < 0$  side of the antenna. For both antennas, good agreement of the antenna radiation resistance and wave dispersion with the model was obtained. It is concluded that unshielded antennas formed from current loops with an important  $|m| = 1$  component for the conditions of our experiment, couple most of their power to the  $m = +1$  helicon mode and thus have negligible parasitic, nonhelicon plasma loading. This result greatly simplifies calculations of power balance in these sources by identifying the helicon as the mode by which energy is transferred to the plasma. © 1999 American Institute of Physics. [S1070-664X(99)02902-X]

## I. INTRODUCTION

The importance of helicon wave produced plasmas in processing of materials<sup>1-7</sup> has made understanding the physical mechanisms involved in this method of plasma production important to the optimization of existing source designs and the design of sources with new applications. Whilst the theory of plasma wave propagation is generally well understood and has enjoyed wide application to radiofrequency heating and current drive in fusion plasma science, the application of plasma wave theory in cold industrial plasma sources produced by helicon waves is relatively new and has not been explored with a theory that includes the geometrical details of the antenna. Consequently, some rather salient facts have evaded careful experimental-theoretical verification. These include that antennas with an  $|m| = 1$  current structure have an excited spectrum that, in most cases but not all, is dominated by one mode: the  $m = +1$  mode. Moreover, under all conditions this mode propagates without a cutoff. There tends to be an absence of  $m = -1$  modes under most conditions.<sup>8,9</sup> Indeed there is even no consensus under what conditions the  $m = -1$  wave may be observed. No clear evidence has been obtained for nonlinear effects in the wave coupling in plasma formation experiments. Finally, the important overriding unanswered question is whether the theoretical antenna radiation resistance agrees with experiment and how much of the antenna power is parasitic (not coupled to the helicon wave). In this paper, we confront

these issues for the case of a cylindrical source with high density ( $n_e \approx 10^{19} - 10^{20} \text{ m}^{-3}$ ) and magnetic field ( $B < 0.2 \text{ T}$ ) and in which the antenna structure is mainly  $|m| = 1$ . The simple geometry makes it possible to use a one-dimensional code for the comparison. Similar detailed comparisons could be explored for the larger size, lower density ( $n_e < 10^{19}$ ) and field sources ( $B_0 < 0.02 \text{ T}$ ) for which the antenna coupling and wave dispersion properties could be quite different, but often these devices have at least two-dimensional geometry. In our experiment, the investigation of  $m = 0$  was hampered by the difficulty of obtaining plasma breakdown with a single  $m = 0$  loop antenna. Despite this, work on plasma formation by  $m = 0$  has been achieved, for example, in a larger plasma using a spiral antenna.<sup>10</sup>

The application of plasma waves to plasma formation as opposed to plasma formation in capacitively coupled plasmas (CCPs) or inductively coupled plasmas (ICPs), benefits from the concept of the antenna radiation resistance. The antenna radiation resistance is calculated in the usual way by applying the induced EMF (electromotive force) method to the volume source current in the antenna.<sup>11</sup> For a bounded plasma, it must always equal the power dissipated in the plasma. For an infinite nondissipative plasma, however, it need only balance the power loss by the Poynting flux at infinity. The antenna radiation resistance is nonzero for wave excitation in an infinite nondissipative medium, but it is zero for CCPs and ICPs in such cases. In the CCP and ICP cases, antenna resistive loading must result from dissipative effects in the plasma. In our case, the plasma cylinder is assumed infinite in at least one direction along the magnetic field axis.

<sup>a)</sup>Electronic mail: gerard.borg@anu.edu.au

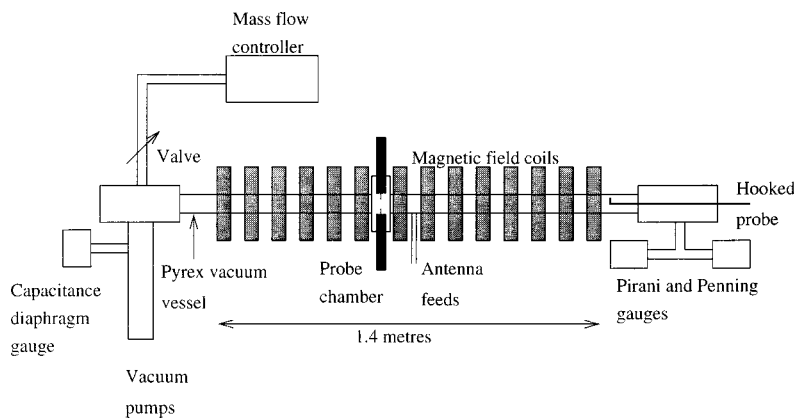


FIG. 1. Experimental layout of the BASIL apparatus showing the 14 axial field coil pancakes. The antenna is located at the axial center of the machine to avoid end effects and extends to the right in the figure. The radial probe guide is located 200 mm to the left of the antenna. All other diagnostics were located to the right of the antenna.

Clearly, the antenna radiation resistance may not depend on the wave dissipation mechanisms in a direct way. Antenna radiation resistance depends primarily on the dispersive properties of the wave and the structure of the antenna. It allows antennas to be designed without regard to what dissipative mechanisms are operational in the plasma. Nonetheless, antenna radiation resistance can still be a measure of the power deposited in a bounded plasma. What is required is that the wave propagates far from the antenna and be damped before returning to the antenna. Whether or not this is the case is usually clear from wavefield measurements. If cavity modes are excited, then the antenna loading depends on the dissipation and dissipative effects cannot be ignored in the calculation of the antenna resistance. Antenna radiation resistance can be measured from the power delivered to the plasma and the current flowing in the antenna without perturbing the plasma, and for devices of one-dimensional geometry like cylindrical geometry, a theoretical calculation of the resistance with a one-dimensional code should be reliable. It should at least determine whether the wave is the main vehicle by which the antenna transmits its power to the plasma as opposed to, say, a parasitic mechanism. In fusion plasma applications in the Alfvén and ion cyclotron frequency ranges (ICRF), the computation of a reliable antenna radiation resistance is not so easy. Problems arise due to the complicated geometry of the machine leading to three-dimensional effects such as toroidal coupling. If there is no electrostatic shield, there are problems due to the unknown proximity of the antenna to the plasma boundary. There may also be antenna driven sheath currents which cause parasitic loading as evidenced either by direct measurement<sup>12</sup> or by nonlinear antenna loading.<sup>13</sup> Evidence now exists that three-dimensional modeling can provide a reliably accurate antenna radiation resistance under some conditions in three-dimensional geometry, but the deficiencies of over-simplified models are recognized.<sup>14</sup>

Modeling of helicon sources is complicated by the wide parameter regime over which helicon waves are used to produce plasmas. In the low density and low field sources ( $B < 0.02$  T and  $n_e < 10^{19} \text{ m}^{-3}$ ), wave-particle interactions have been suggested as being important on occasions in coupling energy into electrons.<sup>15-17</sup> Under these conditions, the effects of finite electron mass are considered to be important.<sup>18,19</sup> It has been argued by Kamenski *et al.*,

however,<sup>11</sup> that for the high density and field sources (even of small radius) considered in this paper, the dominantly excited  $m = +1$  mode is not affected by finite electron mass. According to Shamrai *et al.*,<sup>18</sup> finite electron mass effects are not important for our conditions when  $k_{\perp} < 300 \text{ m}^{-1}$  as satisfied by the  $|m| = +1$  mode. We are therefore justified in using a numerical model which neglects electron mass. Moreover, in the latter sources, the collision mean-free-path is shorter than a wavelength and damping is predominantly due to collisions. As a result, the wave power deposition is local, so that the antenna radiation resistance is the only critical parameter in the energy balance. It should be pointed out that a recent upgrade of the present code to take into account finite electron mass as well as calculations for an infinite homogeneous plasma,<sup>20</sup> appear to indicate that antenna radiation resistance is not strongly dependent on finite electron mass for our experimental conditions.

This paper is structured as follows. In Sec. II we describe the experimental apparatus. In Sec. III we review the physics of the numerical code used to compare with experimental results. In Secs. IV, V, and VI we present, respectively, the experimental results for the double saddle coil and the helical antenna over a wide range of discharge conditions. In Sec. VII we conclude.

## II. APPARATUS

The BASIL experiment is a linear magnetized plasma originally designed as an electrodeless noble gas laser<sup>21</sup> (Fig. 1). The uniform static field is approximately 1.4 m long with a maximum field strength of 0.2 T. The discharge is produced in an axially mounted pyrex tube of 50 mm outside diameter, with the antenna being external to the tube midway along the static field. The magnetic field coils surrounding the tube are located at radius 120 mm. Vacuum is maintained by a diffusion pump, the system having a base pressure of approximately  $1 \mu\text{Torr}$ . Radiofrequency power was provided by a 30 kW PEP CLH30/J AWA broadcast transmitter operated at 7 MHz. Powers up to 10 kW could be coupled to the plasma before arcing at the antenna. High voltage breakdown problems were avoided as much as possible by the use of high voltage vacuum variable capacitors in the match box and delron standoffs for antennas to prevent unipolar arcs chipping the pyrex.

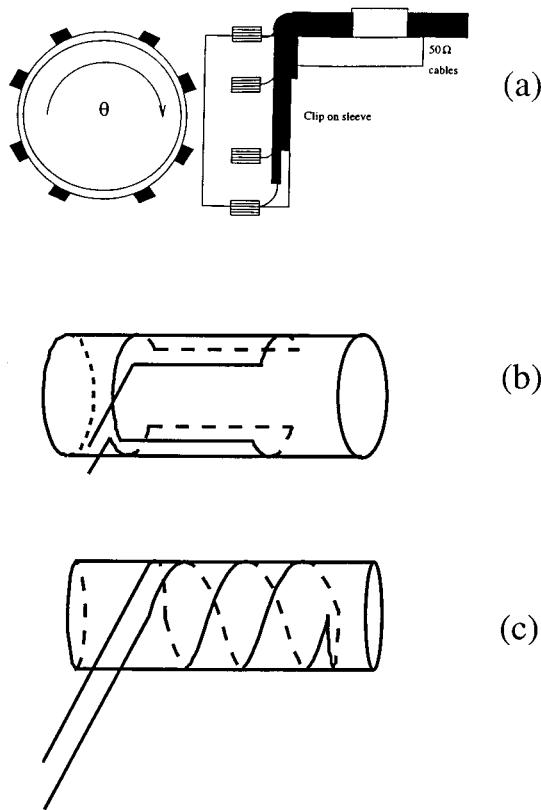


FIG. 2. Diagrams of (a) the azimuthal magnetic  $b_\theta$  probe, (b) the double saddle coil antenna, and (c) the helical antenna.

Radial diagnostic probe access was achieved with a probe chamber 200 mm from the left hand end of the antenna according to Fig. 1, which could support either a radial three-component magnetic probe or a radial Langmuir probe. Axial probe measurements were made with a hooked three-component magnetic probe and Langmuir probe inserted through an O-ring sealed end plate in the vacuum vessel and which could slide along the vessel axis. In order to unambiguously resolve the  $k_\parallel$  and azimuthal mode number spectra, an 8 coil azimuthal magnetic probe array [Fig. 2(a)] sampling  $b_\theta$  was fitted externally to the pyrex tube and could also slide parallel to the vessel axis.

The three-component magnetic probes were orthogonally wound on a single former; each probe having less than 5 mm in linear dimension. All magnetic probe signals have a common mode electrostatic signal capacitively coupled from the plasma. The probes were not shielded but the electrostatic pick-up signal was separated from the magnetic component by a sum and difference network provided by a hybrid combiner.<sup>22,23</sup> The 3-component magnetic probes were calibrated in Helmholtz coils while the azimuthal magnetic probe array was calibrated by clipping onto a short circuited air core coaxial transmission line whose center conductor had the same o.d. as the pyrex vessel and which carried a known current. All rf magnetic probe signals were detected synchronously with the rf drive by a pair of 8 channel, 0.40–40 MHz broadband network analyzers. Antenna radiation resistance is determined by measuring the difference between the forward ( $P_f$ ) and reflected ( $P_r$ ) power into the

matching network and the antenna current ( $I_{ant}$ ) flowing in the antenna. The radiation resistance is then given by

$$R_{rad} = \frac{(P_f - P_r)}{I_{ant}^2} - R_{vac},$$

where  $R_{vac}$  is the so-called vacuum resistance measured in the absence of plasma. An independent test of the radiation resistance measurement was made by placing low inductance resistors of known values across the antenna feeders and comparing their effective series values with the measured impedances.

### III. NUMERICAL MODEL

The results are compared with a numerical code previously employed to assess different antenna types in helicon sources.<sup>11</sup> This model uses the finite element method to solve Maxwell's equations for a cold infinite cylindrical plasma inside a perfectly conducting cylinder with a vacuum gap between the outer conducting boundary and the plasma. The outer conducting boundary corresponds to the inside of the magnetic field coils in BASIL. In the code, the antenna can be placed anywhere inside this cylinder, including in the plasma. The code takes into account nonuniform radial electron density and temperature profiles.

The model uses the  $2 \times 2$  dielectric tensor of a cold collisional plasma, with  $\epsilon_{33} = -\infty$  so that  $E_z = 0$ ,

$$\epsilon = \begin{pmatrix} \epsilon_1 & i\epsilon_2 \\ -i\epsilon_2 & \epsilon_1 \end{pmatrix}, \quad (1)$$

$$\epsilon_1 = 1 - \sum_i \frac{\omega_{pi}^2 (\omega + i\nu_i)}{\omega((\omega + i\nu_i)^2 - \omega_{ci}^2)} - \frac{\omega_{pe}^2 (\omega + i\nu_e)}{\omega((\omega + i\nu_e)^2 - \omega_{ce}^2)}, \quad (2)$$

$$\epsilon_2 = - \sum_i \frac{\omega_{pi}^2 \omega_{ci}}{\omega((\omega + i\nu_i)^2 - \omega_{ci}^2)} + \frac{\omega_{pe}^2 |\omega_{ce}|}{\omega((\omega + i\nu_e)^2 - \omega_{ce}^2)},$$

where  $\omega_{pi}$ ,  $\omega_{pe}$ ,  $\omega_{ci}$ ,  $\omega_{ce}$ ,  $\nu_i$ ,  $\nu_e$  are plasma, cyclotron and collision frequencies for ions and electrons, respectively. The summation in (2) is over all ion species. Different ion species occur when higher order ionization states occur in the same plasma.

The code does not include the effects of finite electron mass. As a result, the code is not capable of describing higher than the first radial mode for the present experimental conditions.<sup>11</sup>

In Sec. II, we compare the observed damping lengths with theory. We cannot use the code to compare the damping rate because of the neglect of the parallel electron dynamics. Instead we simply apply the formulas derived by Chen<sup>24</sup> for the collisional and Landau damping lengths.

### IV. PLASMA FORMATION BY THE DOUBLE SADDLE COIL ANTENNA

A conventional unshielded double saddle coil antenna shown in Fig. 2(b) was wound on a former as a single series-fed element and phased for  $|m| = 1$  excitation. The length of

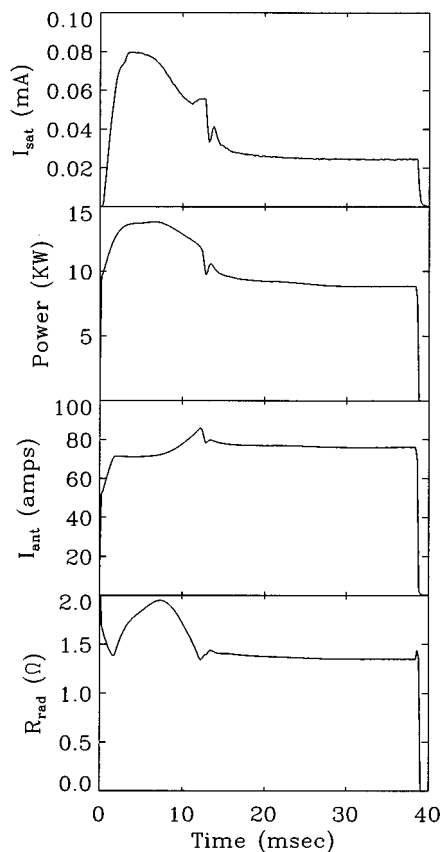


FIG. 3. The time evolution of (a) the density from the ion saturation current, (b) the power into the matching network, (c) the antenna current, and (d) the radiation resistance as a function of time for argon, pressure 30 mTorr, field 0.0896 T with the double saddle coil antenna.

the double saddle antenna is 130 mm and its angular span (the angle of a single azimuthal element subtended at the center of the machine) is  $90^\circ$ .

Figure 3 shows from top to bottom the time evolution of the density (ion saturation current), power, antenna current and antenna radiation resistance during a typical BASIL discharge. The discharge starts with a transient high density phase that later collapses to a lower density. The actual dynamics of the early phase of the discharge has a complex time and axial evolution. From Fig. 3, it can be seen that the power coupled into the plasma drops after the first (high density) phase of the discharge. After the early phase of plasma formation the density becomes quiescent and much more uniform along the tube. Radial magnetic wave field profiles indicate the presence of higher order radial modes in the early phase and predominantly a single radial mode in the quiescent phase. Except for Fig. 8, data in this paper are restricted to the quiescent phase of the discharge.

Measurements were made over a range of parameters with the static magnetic field varied between 0.0384 T to 0.15 T which spans the lower hybrid frequency for argon. Seven sets of radial electron density and temperature profiles, longitudinally scanned azimuthal wave magnetic field and radiation resistance measurements were performed. Figure 4 shows the radial electron density profiles as a function of the static field. These data are for argon, but similar pro-

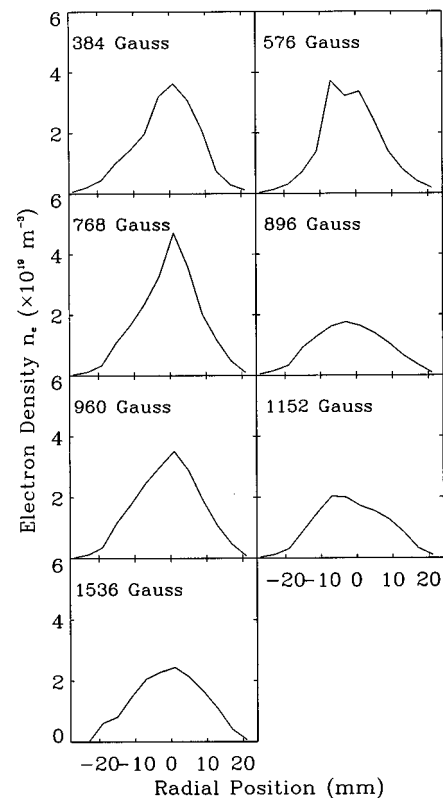


FIG. 4. Radial electron density profiles of an argon discharge with the double saddle coil antenna as the static magnetic field is varied.

files were taken in neon and helium for the dispersion and radiation resistance comparison. A curious phenomenon is that the density is noticeably peaked near 0.0768 T for argon, indicating a change in the plasma dynamics at this point. It will be shown to have no consequence for the agreement between the experimental and the calculated dispersion and antenna radiation resistances.

The azimuthal probe array permitted detailed measurements of the azimuthal and axial wave numbers of the helicon wave. Figure 5 shows a typical azimuthal amplitude and phase profile taken with the 8 coil azimuthal probe 200 mm from the right hand end of the antenna. A deficiency of this probe is that it cannot detect fields with radial nodes at the location of the probe. However, for  $m = \pm 1$  this is not a problem. From the almost linearly increasing phase, the wave is predominantly an  $m = +1$  azimuthal mode. The Fourier series coefficient amplitudes [obtained from a complex expansion in  $\exp(im\theta)$ ] shown as a histogram plot in Fig. 5 confirm this and the striking lack of the  $m = -1$  azimuthal mode. These spectra are qualitatively similar for all axial locations. The radial magnetic wave field profiles in Fig. 6 appear to indicate the dominance of the first radial mode. All the discharges shown in Fig. 4 are very similar in the predominant of an  $m = +1$  azimuthal and first order radial mode in the steady state phase of the discharge. These observations are in qualitative agreement with the code.

For the discharges in Fig. 4, the parallel wave number was determined by Fourier analysis (FFT, fast Fourier transform) of the complex signal (amplitude and phase) from the

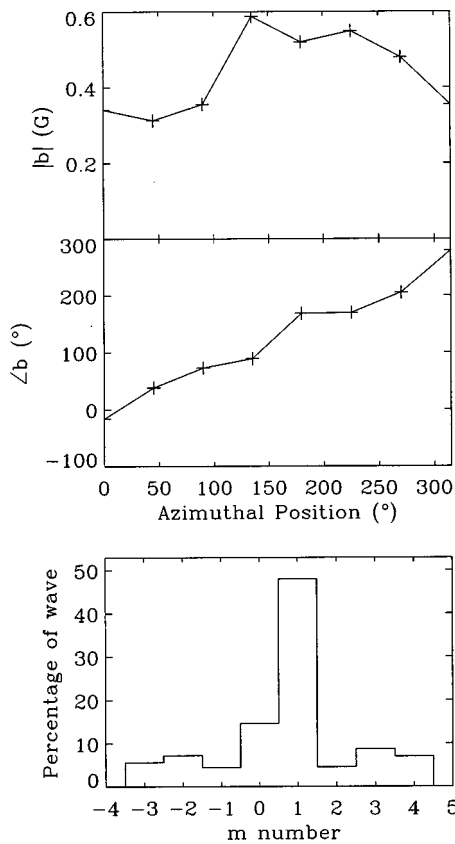


FIG. 5. Azimuthal magnetic wave field (a) amplitude and (b) phase profiles and (c) their Fourier series coefficients for argon, pressure 30 mTorr, field 0.0896 T and  $z=200$  mm from the double saddle coil antenna.

network analyzer of any single element of the azimuthal probe array as it was drawn along the plasma column. To determine whether this was a reliable measurement of the parallel wave number, an on-axis three-component magnetic

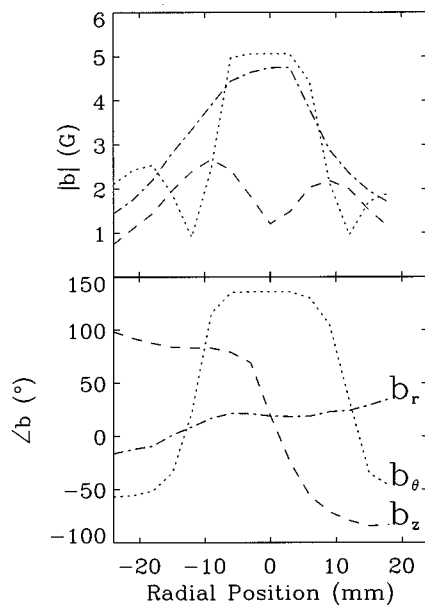


FIG. 6. Radial magnetic wave field profiles of (a) amplitude and (b) phase for argon, pressure 30 mTorr, field 0.0896 T with the double saddle coil antenna.

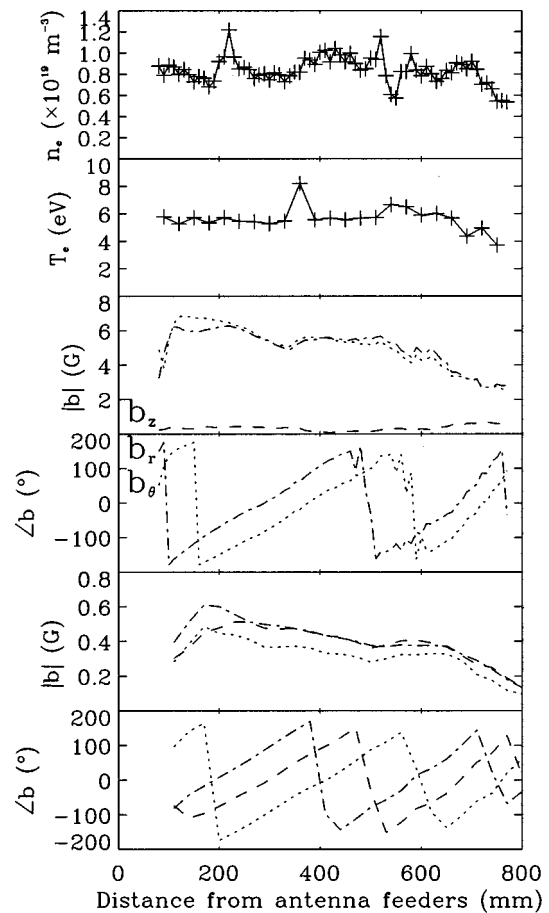


FIG. 7. Axial measurements of (a) electron density and (b) temperature, magnetic wave field, (c) amplitude and (d) phase on axis, and (e) amplitude and (f) phase from the azimuthal probe for argon, pressure 7 mTorr, field 0.1024 T with the double saddle coil antenna 30 ms into the discharge.

probe was used for comparison. This gave similar results, indicating that there were no complicated edge waves like those on resonance cones propagating near the azimuthal probe. This check is very important for helicon waves in the likely presence of the Trivelpiece-Gould mode.<sup>18,19,25,20</sup> An on-axis Langmuir probe was also used to measure the electron density and temperature. The probe was not rf compensated. A discrete Fourier transform (FFT) of this data was chosen to determine the wavenumber because often the slope of the phase varied within a cycle and because the code calculated the spectra of the radiation resistance and the wavefields.

Because the axial probe severely perturbed the plasma under most conditions, the measurements of the axial profile of the on-axis electron density and temperature were only performed at the field for which the plasma was least affected. For this reason, the axial probe was withdrawn from the plasma for the later measurements of the antenna radiation resistance and wavefield dispersion. Figures 7(a) and 7(b) show on-axis axial profiles of the density and temperature for an argon plasma with pressure 7 mTorr and magnetic field 0.1024 T during the steady state phase of the discharge at 30 ms. Figures 7(c) and 7(d) show, respectively, the three components,  $b_r$ ,  $b_\theta$  and  $b_z$  of the on-axis probe and the amplitude of  $b_\theta$  for three probe elements of the azimuthal array.

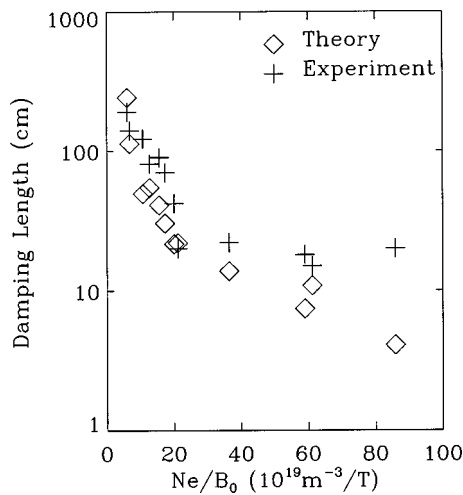


FIG. 8. A comparison between the calculated and experimental estimates of the damping length for a range of plasma conditions. The crosses show the experimental results and the triangles of the theory.

Figure 7(f) shows the phase of the signal detected by the elements of the azimuthal array without the axial probe inserted. This compares well with the phase of the on-axis probe shown in Fig. 7(d).

Figure 8 shows a comparison of the experimental and theoretically calculated damping rates for the same ratios of

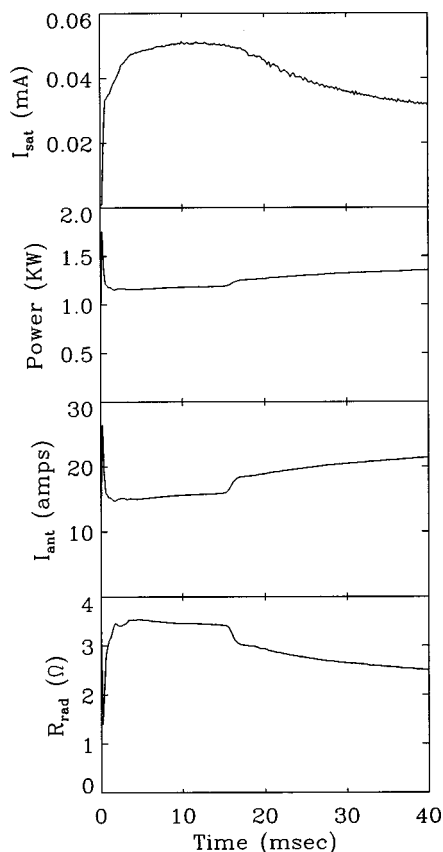


FIG. 9. The time evolution of (a) the density from the ion saturation current, (b) power into the matching network, (c) the antenna current, and (d) the radiation resistance as a function of time for argon, pressure 30 mTorr, field 0.0960 T with the helical antenna.

on-axis density to field that will be used later for the comparisons of dispersion and antenna radiation resistance. Noticeable is the relatively high damping for the higher densities and lower wave damping for the lower densities. In these results, electron-ion and electron-neutral collisions dominate and Landau damping represents less than 15% of the total, even in the low density phase. Most significant is that standing waves reflected at the end of the discharge were not observed. This observation allows the theoretically calculated antenna radiation resistance to be compared with the experimental results.

## V. PLASMA FORMATION WITH THE HELICAL ANTENNA

The helical antenna employed is shown in Fig. 2(c) and has overall length 270 mm and 90 mm distance between turns. The antenna is located between 0 mm and 280 mm, and the elements rotate one and a half times around the discharge in this distance. The helical antenna has a positive helicity,<sup>11,5</sup> strongly coupling to  $k_{\parallel}$ , and azimuthal modes satisfying  $k_{\parallel}/m > 0$ . In the direction along the field where  $k_{\parallel}/m > 0$ , the  $m = +1$  mode should be excited whilst in the direction antiparallel to the field only  $m = -1$  would be allowed to propagate.

The time evolution of the discharge parameters is shown in Fig. 9 and the plasma density profiles for our field scan are shown in Fig. 10. Axial measurements of plasma parameters and the wavefield quantities are shown in Fig. 11 for the steady state phase of the discharge. Measurements on either side of the antenna were accomplished by reversing the static field. The density profile of Fig. 11(a) indicates that the plasma density does not extend far on the  $m < 0$  side of the antenna. On the  $m < 0$  side, the plasma decays away by 100

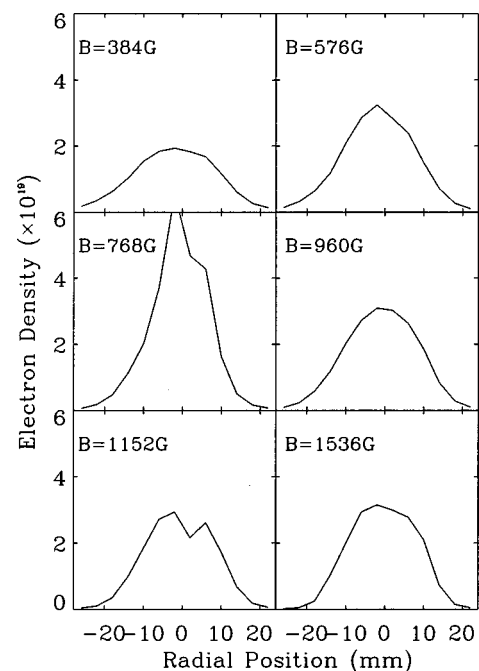


FIG. 10. Radial electron density profiles of an argon discharge with the helical antenna as the static magnetic field is varied.

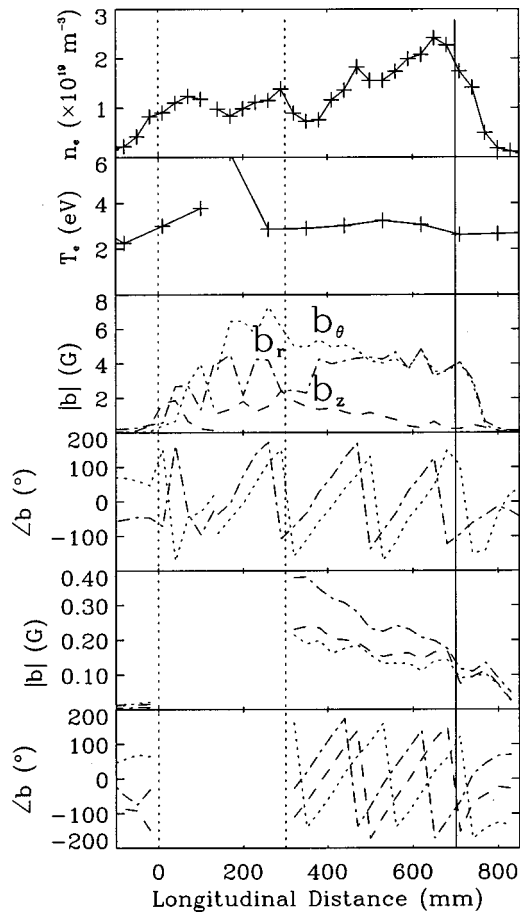


FIG. 11. Axial measurements of (a) electron density and (b) temperature, magnetic wave field, (c) amplitude and (d) phase on axis, and (e) amplitude and (f) phase from three of the azimuthal probes for argon, pressure 30 mTorr, field 0.096 T with a helical antenna at 30 ms into the discharge. The vertical dotted lines show the location of the helical antenna and the vertical unbroken line shows the location of the last magnetic field coil.

mm from the end of the antenna, while on the other  $m > 0$  side, it reaches the end of the static field. The axial and azimuthal magnetic probes show that the wave propagates to the right in the Figure. There is a gradual build up in wave amplitude under the antenna starting from the left end to the right end and then a slight attenuation as the wave propagates down the column.

Figure 12 shows the azimuthal amplitude and the phase profiles for each direction of the static field. The field has the normal positive sense in the right frame of the Figure and the opposite sense in the left frame. These profiles again confirm the dominance of  $m = +1$ . In the right frame the slope is positive and the amplitude is large, indicating a dominant  $m = +1$  mode. Reversal of the static field as shown in the left frame of Fig. 12 causes the wave pattern to rotate in the opposite sense in space compared to the right frame. This is because the sense of azimuthal propagation of a positive azimuthal mode obeys the right hand screw rule with respect to the positive  $z$ -axis (the direction of the steady magnetic field). When the field is reversed so too is the direction of propagation of the  $m = +1$  mode. Thus what we see in the left frame is a low amplitude  $m = +1$  mode (not an  $m = -1$  mode).

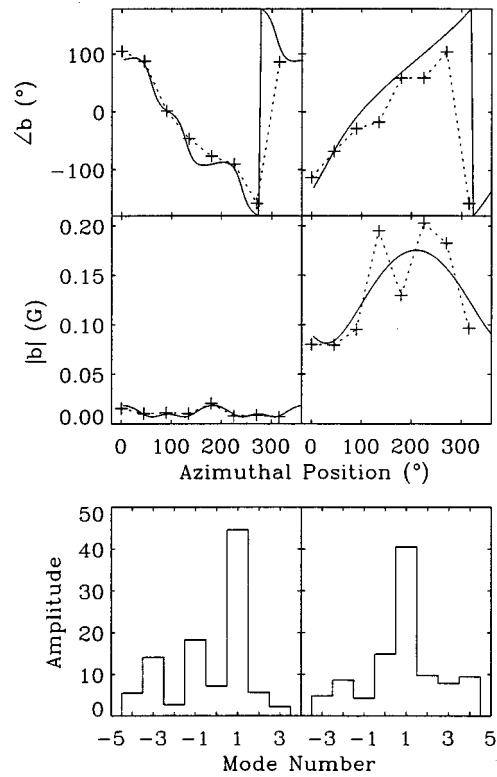


FIG. 12. Azimuthal profiles of the wave fields with corresponding Fourier coefficients for the helical antenna with the magnetic field forward and reversed. The results for the positive direction of the magnetic field are shown at the right. The frames at the left show the profile for the reversed field. Note that in both cases, the field pattern rotates in a right hand sense with respect to the static field.

### VI. COMPARISON OF WAVE DISPERSION AND ANTENNA RADIATION RESISTANCE WITH THE NUMERICAL MODEL

In both the double saddle coil and helical antenna cases the dominant measured wave mode was the  $m = +1$  azimuthal mode. The impedance spectra calculated by the numerical model for the measured plasma conditions show a very high radiation resistance for the  $m = +1$  mode compared to all other modes.<sup>1</sup> A physical explanation for the low excitation efficiency of negative  $m$ -modes is given by Kamenski *et al.*<sup>11</sup> The poor excitation is predominantly due to the central peaking of the density profile, which prevents the  $m = -1$  wavefields from penetrating the bulk of the plasma for these conditions.

The code can calculate the antenna impedance spectrum for various  $(k_{\parallel}, m)$ -mode numbers summed over all radial modes that satisfy the antenna and vessel boundary conditions. One can therefore determine the  $(k_{\parallel}, m)$  of the mode with the largest resistance and wave amplitude. Experimentally one can measure the dominant wavenumber as described above by Fourier transforming (FFT) the axial profile wave data, however, one can only measure the total antenna radiation resistance. Thus, in this section, we compare the measured wavenumbers with the wavenumbers of the dominant mode computed by the code (always  $m = +1$ ) and the measured antenna radiation resistance with the real part of

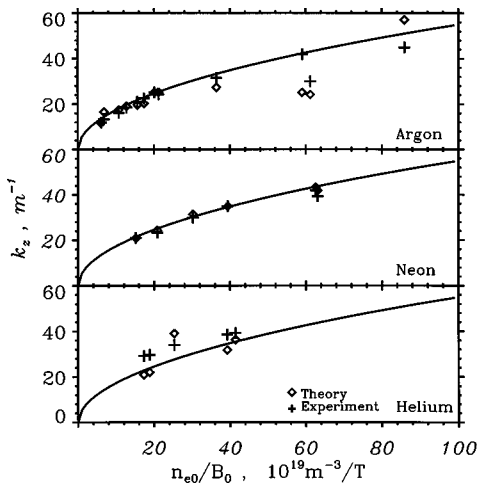


FIG. 13. A comparison between the experimental and numerical model results of the wave dispersion for (a) argon, (b) neon, and (c) helium for a double saddle coil antenna. The parabolic line is a best fit for all cases.

the code calculated antenna impedance integrated over all mode numbers.

Figure 13 compares the measured wavenumbers with those calculated by the code as a function of the ratio of the central density to magnetic field for the double saddle coil antenna. This choice of independent variable is motivated by the simplified dispersion relation for helicon waves<sup>24</sup> which depends uniquely on this ratio according to

$$k_{\parallel}^2 \sqrt{k_{\perp}^2 + k_{\parallel}^2} = \frac{n_e \omega \mu_0 e}{B_0}. \quad (3)$$

This expression is valid for fast waves at frequencies well above the ion cyclotron frequency. Figure 13 shows from top to bottom results for argon, neon and helium plasmas. For argon, the density profiles of Fig. 4 were used in the code. Similar profiles were obtained for neon and helium. The agreement is rather good. The data in Fig. 13 cannot be considered a dispersion relation due to the discontinuous effect that the radial density profiles have on the data. Therefore a theoretical “dispersion relation” cannot be plotted; only the theory points.

Despite this, in Fig. 13 we also plot the simplified dispersion relation,

$$k_{\parallel} = C \sqrt{\frac{n_e}{B_0}}, \quad (4)$$

which is derived from Eq. (3) with  $k_{\perp} \propto k_{\parallel}$ . The constant,  $C$ , is chosen to best fit the data. For the abscissa in units of  $10^{19} \text{ m}^{-3}/\text{T}$ ,  $C \approx 5.5$ . This value is the same for all gases, as would be expected.

It is surprising at first sight that Eq. (4) provides a good general fit to the data. For example, Chen<sup>25</sup> has shown that for a thin machine like BASIL with a conducting wall boundary, the helicon wave boundary condition leads to  $J_1(k_{\perp} a) \approx 0$ , where  $J_1$  is the Bessel function and  $a$  is the wall radius. For the first radial mode in BASIL,  $a = 0.02 \text{ m}$ , and  $k_{\perp}$

$\approx 120 \text{ m}^{-1}$ . Thus,  $k_{\perp} \gg k_{\parallel}$  and from the dispersion relation, Eq. (3),  $k_{\parallel}$  is a linear function of  $n_e/B_0$ . This is clearly in disagreement with Fig. 13. The interpretation previously given by Kamenski and Borg<sup>11</sup> is that the first radial modes of the  $m = \pm 1$  propagate as fast magnetosonic surface waves at low frequencies. These authors provide a discussion of this point and refer the reader to the early work on magnetohydrodynamic (MHD) surface waves in the Alfvén wave heating literature.<sup>22,26,27</sup> The most important consequence is that the  $m = +1$  first radial helicon mode, which is a fast wave mode, does not undergo a waveguide cutoff. Even in a hydrogen plasma at low frequency, machine size and density or at high field, for example, modes like the  $m = 0$  modes or the  $m = +1$  higher radial modes which are body waves undergo waveguide cutoff. This does not occur for the first radial mode of the  $m = +1$  helicon wave. The main surprising result is that contrary to common belief,  $k_{\perp}$  now depends on  $k_{\parallel}$  and is not fixed by the plasma boundary. This result can even be checked for a uniform plasma.

One can apply the definition of a surface wave according to Cross<sup>22</sup> (p. 56). A correspondence between surface waves in a slab and a cylinder has led to the definition of  $k_r^2 = k_{\perp}^2 - m^2/a^2$  for the corresponding effective radial wavenumber in a cylinder. This is a somewhat arbitrary definition but a simple one to employ here. If  $k_r^2 < 0$ , indicating radial evanescence, the wave is a surface wave by definition. From Eq. (3),

$$k_r^2 = \alpha^2/k_{\parallel}^2 - k_{\parallel}^2 - m^2/a^2, \quad (5)$$

where  $\alpha = n_e \omega \mu_0 e / B_0$ . The transition between surface and body wave behavior occurs for  $k_r^2 = 0$  or, approximately,  $(\omega \mu_0 e n_e / k_{\parallel} B_0)^2 - k_{\parallel}^2 = 1/a^2$ . Using the curves in Fig. 13 we may write  $n_e/B_0 (10^{19} \text{ m}^{-3}/\text{T}) \approx 0.0331 k_{\parallel}^2$ . We therefore obtain  $7.6 k_{\parallel}^2 = 1/a^2$  or  $k_{\parallel} < 18 \text{ m}^{-1}$  if  $a = 0.02 \text{ m}$ . Thus, according to this definition, the  $m = +1$  helicon wave at frequencies well above the ion cyclotron frequency is right at the border line of surface wave behavior in a small radius device like BASIL.

In conclusion, we note that even though the experimental data do not prove that the dispersion relation is accurately parabolic, it is clear that the data agree better with a parabola than with a straight line through the origin. For BASIL conditions, the theoretically calculated functional dependence of the dispersion relation agrees with that of Eq. (2) to within a few percent for a constant density profile.

If one gets good agreement in the wavenumber predicted by theory, then the antenna radiation resistance comparison should be a reliable way of revealing the presence of parasitic loading. Figure 14 shows the comparison of the code calculated and the experimentally measured total antenna radiation resistances. The agreement is excellent, at least for the conditions here where the coupling is good. These results are not affected at all by dissipative processes. All that is required is that the wave does not return with significant amplitude to the antenna region after reflection from the ends of the plasma, as previously explained. From Fig. 7, this was indeed the case in BASIL. One can safely conclude that the helicon wave transports the energy launched by the antenna.



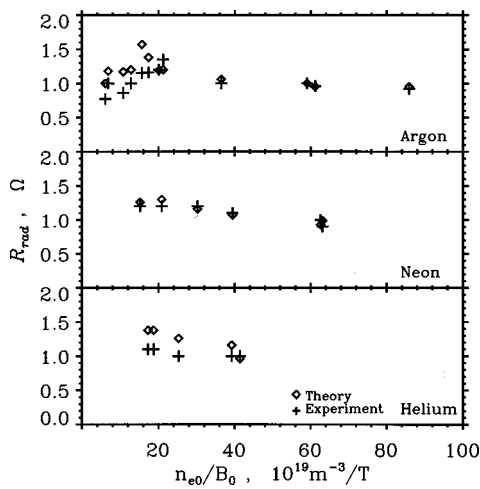


FIG. 14. A comparison between the experimental and model results of the antenna radiation resistance for (a) argon, (b) neon, and (c) helium for a double saddle coil antenna.

Somehow this energy is acquired by the plasma. It is beyond the scope of this paper to examine this question in detail. It should be pointed out, however, that recent calculations with a new code, UFEM,<sup>25</sup> which takes into account the parallel electron dynamics, indicate that it is not obvious that the deposition is localized to the propagating wave but may be concentrated near the antenna elements.

The case of the helical antenna is interesting because of the fact that the plasma only forms on one side of the antenna. Figures 15(a) and (b) show the same results for this case. The wavenumber agreement is again quite reasonable, however, the high wavenumber selectivity of the helical antenna leads to a lower range of observed wavenumbers, even though the same range of fields was used as for the double saddle coil antenna. The antenna radiation resistance agreement is satisfactory, except at low fields, where the experimental results are higher than theory. This cannot suggest a slight parasitic loading since the same effect would have

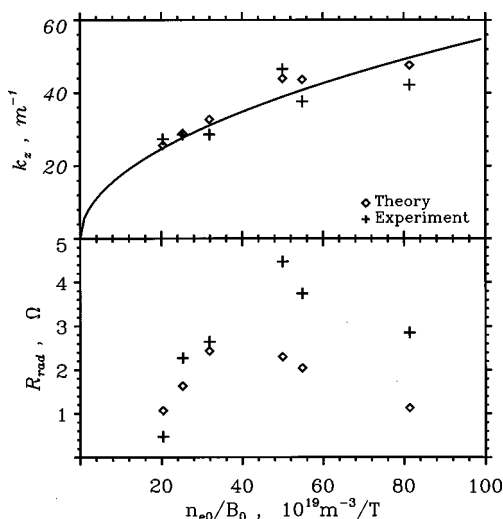


FIG. 15. A comparison between the experimental and model results of the wave dispersion antenna radiation resistance in argon plasma for the helical antenna. (a) Dispersion; (b) antenna radiation resistance.

been evident in the double saddle coil results. We have been unable to satisfactorily resolve this discrepancy, even by use of the UFEM code and putting a reflector on the  $m = -1$  side of the antenna in the code in order to simulate the absence of plasma density on the  $m = -1$  side of the antenna.

To the best of the authors' knowledge, this is the first comparison of the helicon wave dispersion and antenna radiation resistance in a high density and field helicon wave driven source that is free of adjustable parameters. A similar detailed comparison of the dispersion relation has been performed by Davies and Christiansen<sup>28</sup> for the case of a low density ( $n_e < 5 \times 10^{17} \text{m}^{-3}$ ) and field ( $B_0 < 0.04 \text{T}$ ) preformed plasma. According to these authors, the effects of finite electron mass cannot be neglected for the prediction of the dispersion relation as they could in our case. This conclusion appears to agree with more recent work.<sup>18,19</sup>

### VII. SUMMARY AND CONCLUSION

Detailed wavefield measurements and a numerical code comparison have demonstrated that the helicon wave launched by both a double saddle coil and a helical antenna in the high density, high field machine BASIL is composed almost exclusively of the  $m = +1$  mode. An attempt to force coupling to  $m < 0$  modes by the positive helicity, helical antenna proved unsuccessful and an asymmetric plasma formed with the plasma extending only a short distance in the  $m < 0$  direction from the antenna. This confirmed the poor coupling of  $m < 0$  modes predicted by the numerical code for our conditions.

For both antennas, good agreement was found between experimental measurements of the wave dispersion and the antenna radiation resistance and the results of the numerical code. This justifies the neglect of finite electron mass (implying  $E_z = 0$ ) by the code for the calculation of dispersion and antenna radiation resistance for our conditions. We conclude that there are negligible power losses through parasitic effects such as those which account for all the coupling in capacitively and inductively coupled discharges; at least whenever there is good coupling to a helicon mode.

It is interesting to note by comparison of Figs. 3 and 9 that the power employed to create a given density is significantly higher for the double saddle coil than for the helical antenna; the helical antenna requiring, at most, 1.5 kW whereas the double saddle coil requires up to 8 kW. This is partly due to the fact that the helical antenna only produces a plasma along half the length of the tube. In fact, there are additional effects that need to be considered. The study of the antenna radiation resistance is but a first, simple step toward a complete understanding and quantification of the helicon discharge physics.

### ACKNOWLEDGMENTS

The authors are pleased to acknowledge discussions with Dr. D. G. Miljak, Dr. R. W. Boswell, and Dr. A. W. Degeling.

One of the authors (G.G.B.) is grateful for the support of a QEII fellowship.

- <sup>1</sup>R. W. Boswell and D. Henry, *Appl. Phys. Lett.* **47**, 1095 (1985).
- <sup>2</sup>A. J. Perry and R. W. Boswell, *Appl. Phys. Lett.* **55**, 148 (1989).
- <sup>3</sup>A. J. Perry, D. Vender, and R. W. Boswell, *J. Vac. Sci. Technol. B* **9**, 310 (1991).
- <sup>4</sup>S. Shinohara, Y. Miyauchi, and Y. Kawai, *Plasma Phys. Controlled Fusion* **37**, 1015 (1995).
- <sup>5</sup>T. Shoji, Y. Sakawa, S. Nakazawa, K. Kadota, and T. Sato, *Plasma Sources Sci. Technol.* **2**, 5 (1993).
- <sup>6</sup>M. A. Lieberman and R. A. Gottscho, *Physics of Thin Films* (Academic, New York, 1994).
- <sup>7</sup>M. Light and F. F. Chen, *Phys. Plasmas* **2**, 1084 (1995).
- <sup>8</sup>F. F. Chen, I. D. Sudit, and M. Light, *Plasma Sources Sci. Technol.* **5**, 173 (1996).
- <sup>9</sup>G. G. Borg, D. A. Schneider, and I. V. Kamenski, *Bull. Am. Phys. Soc.* **40**, 1697 (1995).
- <sup>10</sup>S. Shinohara, S. Takechi, N. Kaneda, and Y. Kawai, *Plasma Phys. Controlled Fusion* **39**, 1479 (1997).
- <sup>11</sup>I. V. Kamenski and G. G. Borg, *Phys. Plasmas* **3**, 4396 (1996).
- <sup>12</sup>G. G. Borg and B. Joye, *Nucl. Fusion* **32**, 801 (1992).
- <sup>13</sup>D. W. Swain, R. I. Pinsker, F. W. Baity, M. D. Carter, J. S. deGrassie, E. J. Doyle, G. R. Hanson, K. W. Kim, R. A. Mover, and C. C. Petty, *Nucl. Fusion* **37**, 211 (1997).
- <sup>14</sup>M. D. Carter, D. A. Rasmussen, P. M. Ryan, G. R. Hanson, D. C. Stallings, D. B. Batchelor, T. S. Bigelow, A. C. England, D. J. Hoffman, M. Murakami, C. Y. Wang, J. B. Wilgen, J. H. Rogers, J. R. Wilson, R. Majeski, and G. Schilling, *Nucl. Fusion* **36**, 209 (1996).
- <sup>15</sup>A. R. Ellingboe, R. W. Boswell, J. P. Booth, and N. Sadeghi, *Phys. Plasmas* **2**, 1807 (1995).
- <sup>16</sup>P. K. Loewenhardt, B. D. Blackwell, R. W. Boswell, G. D. Conway, and S. M. Hamberger, *Phys. Rev. Lett.* **67**, 2792 (1991).
- <sup>17</sup>A. W. Degeling, C. O. Jung, R. W. Boswell, and A. R. Ellingboe, *Phys. Plasmas* **3**, 2788 (1996).
- <sup>18</sup>K. P. Shamrai and V. B. Taranov, *Plasma Sources Sci. Technol.* **5**, 474 (1996); K. P. Shamrai and V. B. Taranov, *Plasma Phys. Controlled Fusion* **36**, 1719 (1994).
- <sup>19</sup>F. F. Chen and D. Arnush, *Phys. Plasmas* **4**, 3411 (1997).
- <sup>20</sup>G. G. Borg and R. W. Boswell, *Phys. Plasmas* **5**, 564 (1998).
- <sup>21</sup>P. Zhu and R. W. Boswell, *Phys. Rev. Lett.* **63**, 2805 (1991).
- <sup>22</sup>R. C. Cross, *An Introduction to Alfvén Waves* (Adam Hilger, Bristol, 1988).
- <sup>23</sup>G. G. Borg and T. Jahreis, *Rev. Sci. Instrum.* **65**, 449 (1994).
- <sup>24</sup>F. F. Chen, *Plasma Phys. Controlled Fusion* **33**, 339 (1991).
- <sup>25</sup>I. V. Kamenski and G. G. Borg, "A 1D cylindrical kinetic code for helicon plasma sources," submitted to *Comput. Phys. Commun.*
- <sup>26</sup>M. J. Ballico and R. C. Cross, *Plasma Phys. Controlled Fusion* **31**, 1141 (1989).
- <sup>27</sup>G. A. Collins, N. F. Cramer, and I. J. Donnelly, *Plasma Phys. Controlled Fusion* **28**, 597 (1986).
- <sup>28</sup>B. Davies and P. J. Christiansen, *Plasma Phys.* **11**, 987 (1969).